CHINESE OPTICS LETTERS

Vol. 21, No. 7 | July 2023

Spectral-furcated vector soliton in birefringence-managed fiber lasers

Zhiwen He (贺志文), Dong Mao (毛 东)*, Yueqing Du (杜岳卿), Qun Gao (高 群), Chao Zeng (曾 超), Changchi Yuan (袁昌驰), and Jianlin Zhao (赵建林)

Key Laboratory of Light Field Manipulation and Information Acquisition, Ministry of Industry and Information Technology; Shaanxi Key Laboratory of Optical Information Technology; School of Physical Science and Technology, Northwestern Polytechnical University, Xi'an 710072, China

*Corresponding author: maodong@nwpu.edu.cn

Received February 14, 2023 | Accepted April 14, 2023 | Posted Online July 12, 2023

We demonstrate spectral-furcated vector solitons in normal-dispersion fiber lasers comprising a section of polarization-maintaining fiber. The spectrum of each orthogonal-polarized component is confined by the birefringence-related phase-matching principle, and the bicorn spectral structure corresponds to the zero-order sidebands of two vector modes. Due to the Hopf bifurcation effect, the vector soliton evolves into a breathing state at the higher pump level, accompanied by an extra set of sub-sidebands that continuously exchange energy with the zero-order sidebands. Simulation results fully reproduce experimental observations of the spectral furcation and soliton breathing, offering comprehensive insights into the pulse-shaping mechanism of the birefringence-managed soliton.

Keywords: fiber laser; soliton; bicorn spectral structure; birefringence management.
DOI: 10.3788/COL202321.071402

1. Introduction

Soliton, whose solitary wave owning robustness over a long propagation distance, has been intensively investigated in various fields ranging from Bose–Einstein condensates[1], plasma[2], hydro dynamics[3], laser sensing[4,5], to optics communications[6]. In dissipative optical systems, soliton formation is generally governed by the coaction of chromatic dispersion and nonlinearity, together with gain and loss[7], and the fiber laser serves as an excellent platform for exploring intriguing phenomena of optical solitons[8]. Hitherto, through engineering the net cavity dispersion of the fiber laser, researchers have demonstrated a chirp-free conventional soliton[9] in the anomalous-dispersion regime, the weakly chirped dispersion-managed soliton[10] in the near-zero-dispersion regime, as well as the giant-chirped self-similar pulse[11,12] and the dissipative soliton[7,13] in the normal-dispersion regime.

Initially, solitons emitted from fiber lasers are usually treated as scalar ones, despite that a single-mode fiber (SMF) can support two orthogonal-polarized components[14]. The vector nature of solitons was theoretically predicted by Menyuk in 1987, where two orthogonal-polarized components trapped each other through a reverse central frequency shift and formed a robust vector soliton in the anomalous-dispersion SMF[15]. Following this discovery, various types of vector solitons have been demonstrated in fiber lasers by adjusting the cavity birefringence and mode-coupling strength between the two orthogonal-polarized components, including the group-velocity-locked vector solitons[16,17], polarization-locked vector solitons[18–20], and polarization-rotation vector solitons[21,22].

Recently, it was demonstrated that when a section of polarization-maintaining fiber (PMF) was incorporated into the cavity, even the normal-dispersion fiber laser could directly emit the near-chirp-free birefringence-managed soliton (BMS)[23,24]. Though the conventional solitons[25] and BMS exhibit similar spectral profiles with pairs of sharp sidebands, they possess distinct formation mechanism and evolution behaviors. For instance, the conventional soliton stems from the balance of self-phase modulation and anomalous dispersion, while the BMS originates from the combined action of the birefringence-related phase-matching principle and normal dispersion. In comparison to the vector solitons achieved in anomalous-dispersion fiber lasers[18], the two orthogonal-polarized components of the BMS possess asymmetric spectral profiles with evidently distinct central wavelengths and sideband positions. Despite the fact that the basic characteristics of the BMS have been recently revealed, further studies are needed to explore more intriguing properties of this brand new pulse in fiber lasers.

In this work, we numerically and experimentally demonstrate the spectral-furcated BMS (SF-BMS) in a normal-dispersion birefringence-managed fiber laser, which displays a bicorn structure on the spectrum. Each orthogonal-polarized component has an asymmetric spectral profile with strong sidebands originating from the birefringence-related phase-matching

effect. Due to unequal mode coupling between the two vector modes, the zero-order sideband of each component grows up quickly from the spectral peak, giving rise to the unique vector soliton with the bicorn spectrum. Under higher pump levels, the vector soliton evolves into a breathing state due to the Hopf bifurcation effect, accompanied by the continuous energy exchange between sub-sidebands and zero-order sidebands. The experimental results qualitatively support the numerical simulations, corroborating that the unequal mode-coupling and birefringence-related phase-matching effect play significant roles in the formation of the bicorn spectrum. Our work reveals the formation mechanism and properties of the SF-BMS, providing a deeper understanding of the birefringence-related soliton-shaping mechanism.

2. Experimental Setup and Simulation Model

The schematic of the birefringence-managed laser is shown in the left panel of Fig. 1(a). A 980 nm laser diode pumps the 7.2 m erbium-doped fiber (EDF, EDFC 980 HP) through an optical integrated module, which acts as the wavelength division multiplexer, the polarization-independent isolator, and the output coupler with a 30% output ratio. A 1-m PMF (PM1550XP)

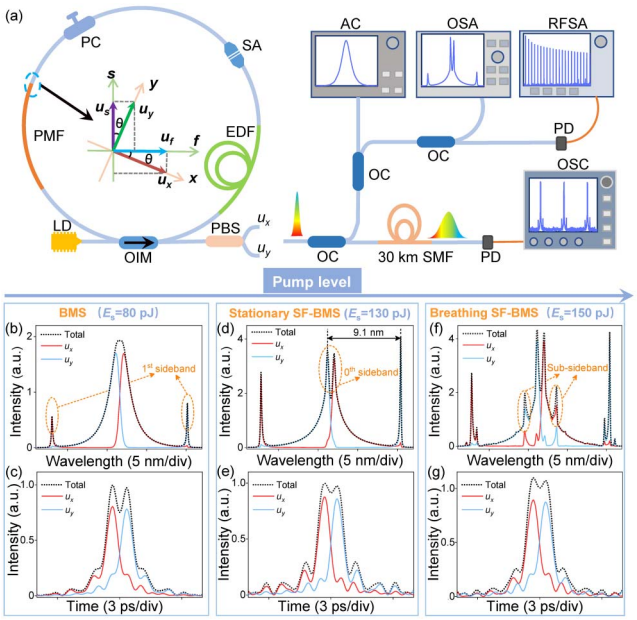

Fig. 1. Laser setup and evolution of BMS to SF-BMS. (a) The configuration and measuring system of the fiber laser. The simulated spectra and pulses for gain saturation energy of (b),(c) 80 pJ, (d),(e) 130 pJ, and (f),(g) 150 pJ. LD, laser diode; OIM, optical integrated module (performs the roles of the polarization-independent isolator, the wavelength-division multiplexer, and the optical coupler); EDF, erbium-doped fiber; SA, saturable absorber; PC, polarization controller; PMF, polarization-maintaining fiber; PBS, polarization beam splitter; OC, optical coupler; AC, autocorrelator; OSA, optical spectrum analyzer; RFSA, radio frequency spectrum analyzer; PD, photodetector; OSC, oscilloscope.

introduces high birefringence into the cavity, and the intra-cavity polarization state is tuned via a polarization controller. Moreover, the carbon nanotube saturable absorber enables the passive mode locking of the fiber laser. The pigtails of all components comprise a SMF (SMF-28e$^+$), and the cavity length is about 9.2 m. The dispersion parameters of SMF, PMF, and EDF are 17 ps, 17 ps, and $-16.5\,\mathrm{ps(nm\cdot km)^{-1}}$, respectively, giving the net-cavity dispersion of $\sim 0.11\,\mathrm{ps}^2$.

The right panel of Fig. 1(a) displays the measurement system. At the output terminal of the fiber laser, a polarization beam splitter resolves the pulse into two orthogonal-polarized components. Subsequently, an autocorrelator (Pulsecheck, USB-150), an optical spectrum analyzer (YOKOGAWA, AQ6370), and a radio frequency spectrum analyzer (Agilent, E4440 A) are used to monitor the properties of the pulses. The combination of a 30 km SMF, a 5 GHz photodetector (THORLABS, DET09CFC/M), and a 4 GHz oscilloscope (Lecroy, 740Zi-A) comprises the dispersive Fourier transform system, in which the real-time spectral resolution is calculated as ~0.48 nm.

Numerical simulations are performed to study the formation of the vector pulse in the birefringence-managed fiber laser. The lumped propagation model is employed, which treats fiber components as separate transmission functions[26,27]. Considering the non-negligible difference of birefringence between the SMF and the PMF, the mode coupling on the connection point should be specially considered [inset of Fig. 1(a)], which can be expressed as[23]

$$[u_f\ u_s] = [u_x\ u_y]\begin{bmatrix}\cos\theta & -\sin\theta\\ \sin\theta & \cos\theta\end{bmatrix}, \tag{1}$$

where u_f and u_s denote fast and slow components along the PMF, while u_x and u_y represent that along the SMF, respectively. θ is the polarization orientation angle between the fast components in SMF and PMF. At the output terminal of the PMF, θ is set as zero so that u_f (u_s) component in the PMF converts into the u_x (u_y) component in the SMF.

The pulse propagation in the cavity can be described using the coupled Ginzburg–Landau equations expressed as Eq. (2), which considers the birefringence, nonlinearity, and dispersion, together with gain and loss[19,23],

$$\begin{aligned}\frac{\partial u_x}{\partial z} &= -i\beta u_x + \delta\frac{\partial u_x}{\partial t} - i\frac{k_2}{2}\frac{\partial^2 u_x}{\partial t^2} + i\gamma\left(|u_x|^2 + \frac{2}{3}|u_y|^2\right)u_x \\ &\quad + \frac{i\gamma u_y^2 u_x^*}{3} + \frac{(g-\alpha)}{2}u_x + \frac{g}{2\Omega_g^2}\frac{\partial^2 u_x}{\partial t^2},\\ \frac{\partial u_y}{\partial z} &= i\beta u_y - \delta\frac{\partial u_y}{\partial t} - i\frac{k_2}{2}\frac{\partial^2 u_y}{\partial t^2} + i\gamma\left(|u_y|^2 + \frac{2}{3}|u_x|^2\right)u_y \\ &\quad + \frac{i\gamma u_x^2 u_y^*}{3} + \frac{(g-\alpha)}{2}u_y + \frac{g}{2\Omega_g^2}\frac{\partial^2 u_y}{\partial t^2},\end{aligned} \tag{2}$$

where u_x and u_y are the envelopes of the two orthogonal-polarized components, t corresponds to the retard-time, and z relates to the cavity position. Δn, $2\beta = 2\pi\Delta n/\lambda$, and $2\delta = 2\beta\lambda/2\pi c$

describe the differences of the refractive index, wave number, and inverse group velocity between two orthogonal-polarized components, respectively. k_2 denotes the dispersion coefficient, α represents the loss, and γ is the fiber nonlinear coefficient. $g = g_0 \exp(-E_p/E_s)$ is the saturable gain, where E_p, g_0, and E_s correspond to the pulse energy, small-signal gain coefficient, and gain saturation energy, respectively. Ω_g relates to the gain bandwidth. The saturable absorber is modeled by $T = 1 - \alpha_{NS} - \alpha_S/[1 + P_{(\tau)}/P_{sat}]$, where α_{NS} is the non-saturable loss, α_S is the modulation depth, $P_{(\tau)}$ is the instantaneous power, and P_{sat} is the saturation power.

The split-step Fourier method is utilized to solve Eq. (2), and the simulation parameters are set as follows: $\lambda = 1560$ nm, $\Omega_g = 25$ nm, $\alpha_{NS} = 0.57$, $\alpha_S = 0.07$, and $P_{sat} = 8$ W. For the 1-m SMF, $g_0 = 0$, $k_2 = -21.9\ \mathrm{ps^2\ km^{-1}}$, $\Delta n = 1.5 \times 10^{-6}$, and $\gamma = 1\ \mathrm{W^{-1}\ km^{-1}}$. For the 7.2-m EDF, $g_0 = 0.7\ \mathrm{m^{-1}}$, $k_2 = 21.3\ \mathrm{ps^2\ km^{-1}}$, $\Delta n = 1.5 \times 10^{-6}$, and $\gamma = 3\ \mathrm{W^{-1}\ km^{-1}}$. For the 1-m PMF, $\Delta n = 3.6 \times 10^{-4}$ and other parameters are identical to that of the SMF. For the typical BMS, the stationary SF-BMS, and the breathing SF-BMS, the gain saturation energies are set to 80 pJ, 130 pJ, and 150 pJ, respectively.

3. Simulation Results of the SF-BMS

Starting from a low-intensity noise pulse and fixing θ at 0.15π, the simulation results mainly rest with the gain saturation energy E_s. The SF-BMS can be obtained when the PMF length ranges from 0.85 to 1.1 m, and here we choose the PMF length of 1 m as the typical state. The lower panel of Fig. 1 shows three typical operations of the BMS. The formation of the BMS can be attributed to the birefringence-related phase-matching effect that includes strong birefringence, fiber nonlinearity, and normal dispersion[23,24]. For $E_s = 80$ pJ, the fiber laser emits typical BMS, as shown in Figs. 1(b) and 1(c). The BMS comprises two orthogonal-polarized components, and both of them exhibit asymmetric spectral profiles with sharp sidebands. The bandwidth of each component is ~1.6 nm, which is much larger than their spectral separation of ~1 nm, thus the total BMS has one spectral center. In the temporal domain, the total pulse is the superposition of two orthogonal-polarized components without shift, and it displays a concave shape. Furthermore, oscillating tails appear on the BMS and its two constituents, which result from the interference between soliton and sidebands, somewhat similar to that of the conventional soliton achieved in anomalous-dispersion regimes[28,29].

When E_s reaches 130 pJ, the bandwidth of each component decreases to ~0.8 nm, which is comparable to their spectral separation of ~0.85 nm. Hence, a unique bicorn structure emerges around the central region of the spectrum, as shown in Fig. 1(d). It is evident that the intensity of the sidebands increases with the E_s, akin to the conventional solitons that stronger perturbations lead to larger Kelly sidebands[25]. Compared with the pulse profile in Fig. 1(c), the temporal concave in Fig. 1(e) becomes less evident since the temporal separation between two orthogonal-polarized components decreases from ~0.72 to ~0.60 ps. The breathing SF-BMS can be obtained by further increasing E_s to 150 pJ, and an extra set of sub-sidebands symmetrically appear on both sides of the spectrum, as denoted by the orange circles in Fig. 1(f). Such sub-sidebands arise from the intracavity modulation instability, and similar sub-sidebands have been observed on the spectra of breathing conventional solitons[30].

Such solitons in the laser system experience the Hopf bifurcation with the increase of E_s, as shown in Fig. 2(a). For E_s below 133 pJ, the pulse energy has a fixed value, which corresponds to the stationary SF-BMS. When E_s is higher than 133 pJ, the bifurcation occurs, and the pulse energy oscillates between two divergent values, i.e., breathing dynamics. The temporal and spectral evolution of the breathing SF-BMS over 100 round-trips (RTs) are plotted to uncover the underlying dynamics. As illustrated by the autocorrelation evolution in Fig. 2(b), the temporal concave appears and disappears regularly, accompanied by the periodically varying separation between the oscillating tail and center of the pulse. This evolution behavior corresponds to the periodic change in the temporal separation between two orthogonal-polarized components of SF-BMS, which can be attributed to the normal dispersion and the varying spectral centroid separation of two components [Fig. 2(c)]. Correspondingly, the spectra depicted in Fig. 2(d) evolve with a period of 10 RTs, and the spectral variation mainly focuses on the bicorn structure and the sub-sidebands [Fig. 2(e)]. As shown in Fig. 2(f), the peak intensity of the sub-sidebands (peak P_1 and peak P_4) decreases while that of the bicorn structure (peak P_2 and peak P_3) increases, and vice versa. This evolving

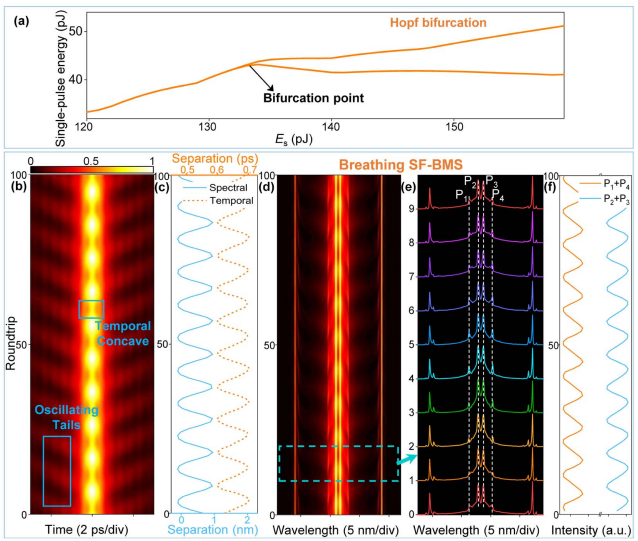

Fig. 2. Hopf bifurcation property of the laser system. (a) The bifurcation diagram versus the gain saturation energy. (b) The autocorrelation evolution over 100 RTs. (c) The temporal separation and spectral centroid separation between the two components over 100 RTs. (d) The spectral evolution over 100 RTs. (e) The concrete spectra of the breathing SF-BMS over 10 RTs. (f) The peak intensity evolution of the bicorn structure (blue line) and the sub-sidebands (orange line) over 100 RTs.

behavior is indicative of a continuous energy exchange between the bicorn part and the sub-sidebands, which promotes the dynamic balance of the breathing SF-BMS. Besides, the breathing period of the SF-BMS can be increased by further enhancing the gain saturation energy. Note that the maximum gain saturation energy for maintaining the SF-BMS operation is about 360 pJ. Otherwise, the laser will evolve into a chaotic state.

4. Origination of the Bicorn Spectrum

In our previous work[23], we have demonstrated that in a normal-dispersion birefringence-managed fiber laser, near-chirp-free BMSs can be obtained when θ ranges from 0.1π to 0.4π. When the BMS circulates inside the cavity, new frequencies will be generated and propagate at their own velocities due to the periodical perturbations including gain, loss, and mode-coupling[23,24]. A phase difference is induced between the central frequency and newly emerged frequency per roundtrip, which is ascribed to the coaction of birefringence, normal dispersion, and nonlinearity. Then, the resonant sideband appears at the frequency where the phase-matching principle is satisfied,

$$\Delta\omega_x = \frac{b \pm \sqrt{b^2 + 4a(\phi_{nlx} + 2m\pi)}}{2a},$$
$$\Delta\omega_y = \frac{-b \pm \sqrt{b^2 + 4a(\phi_{nly} + 2m\pi)}}{2a},$$
$$a = \frac{1}{2}\sum_i k_{2i}L_i, \quad b = \frac{1}{2c}\sum_i \Delta n_i L_i, \tag{3}$$

where $\phi_{nlx/y}$ represents the nonlinear phase shift, and m is the order of the sidebands. $\Delta\omega_{x/y}$ is the frequency offset between the sideband and central wavelength of each orthogonal-polarized component. For the two components propagating in the fiber with the length of L_i, Δn_i describes the refractive index difference, and k_{2i} denotes the group velocity dispersion. Based on the simulation parameters, real solutions of Eq. (3) can always be obtained when $m \geq 0$, implying the existence of the zero-order sidebands. Taking the u_y component in Fig. 1(d) as an example, the nonlinear phase shift ϕ_{nly} is estimated to be ~0.08 based on the peak intensity and nonlinear coefficient. On this basis, the spectral separation between the zero-order and the first-order sidebands is calculated as ~9 nm, which is consistent with the simulated results of ~9.1 nm in Fig. 1(d).

Figures 3(a) and 3(b) display the spectral evolution of the SF-BMS as a function of E_s, in which the separation between the zero-order sidebands of the two components increases with E_s [orange symbol line in Fig. 3(a)], coinciding with the phase-matching principle that the stronger nonlinear phase shift leads to a larger frequency offset between the central frequency and sidebands[23]. Notably, the bicorn spectral structure becomes more prominent because the ratio between the spectral separation and the bandwidth of the u_x component increases with the enhancement of E_s [magenta symbol line in Fig. 3(a)].

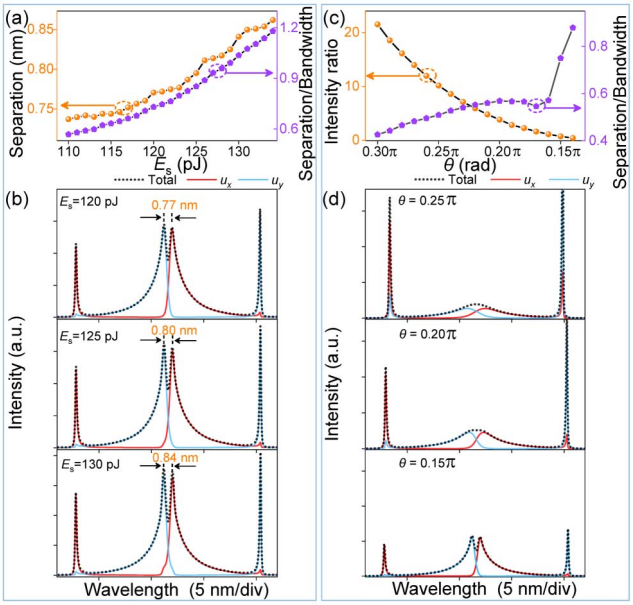

Fig. 3. Spectral evolution versus gain saturation energy (left column) and polarization orientation angle (right column). (a) The spectral separation between two peaks of the bicorn structure (orange symbol line), and the ratio between the spectral separation and bandwidth of the u_x component (magenta symbol line) versus the E_s. (b) Three typical spectra for θ of 0.15π but with different E_s. (c) The intensity ratio between the first-order sideband and the spectral center (orange symbol line), and the ratio between the spectral separation and bandwidth of the u_x component (magenta symbol line) versus θ. (d) Three typical spectra for the E_s of 120 pJ but with different θ.

Figures 3(c) and 3(d) exhibit the spectral evolution of the BMS with respect to θ. For E_s of 120 pJ, the intensity ratio between the first-order sideband and spectral center decreases monotonically with the increase of θ [orange symbol line in Fig. 3(c)]. This observation agrees with our previous result[23], which can be understood as that a smaller θ contributes to a smaller variation of the pulse property, i.e., the weaker perturbation. The magenta symbol line in Fig. 3(c) illustrates the evolution of the ratio between the spectral separation and the bandwidth of the u_x component, which basically increases with the reduction of θ. Accordingly, the bicorn spectrum is prone to appear for the certain range of 0.14π to 0.2π (corresponding to unequal polarization mode coupling), and it becomes more evident for θ of $\sim 0.15\pi$.

Therefore, it can be concluded that the bicorn structure at the spectral center of SF-BMS essentially corresponds to the sufficiently amplified zero-order sidebands of each orthogonal-polarized component, which arise from the birefringence-related phase-matching effect. Ascribed to the unequal mode coupling occurring for small θ, most of the energy is concentrated in the central region of the spectrum, which greatly enhances the zero-order sidebands around the central wavelength of each component. On this basis, with the increase of E_s, the zero-order sidebands can be enhanced easily from the central peak of each component, thereby manifesting as the bicorn spectral structure in the central region of the SF-BMS.

5. Experimental Results of the SF-BMS

The simulation results can be experimentally verified in the fiber laser. At the pump power of 22.6 mW, the typical BMS exhibiting only one peak in the spectral center is achieved, as shown in Figs. 4(a)–4(c). By increasing the pump power to 29 mW, the bicorn structure emerges in the central region of the spectrum [Figs. 4(d)–4(f)]. The separation between the zero-order and first-order sidebands of the u_y component is found to be ∼9.2 nm, agreeing well with the simulated result of ∼9.1 nm in Fig. 1(d). The radio frequency spectra of the BMS and the stationary SF-BMS are depicted in Figs. 4(c) and 4(f), respectively. The fundamental repetition rates of the stationary SF-BMS and its two components are 22.397 MHz, coinciding with the cavity length of ∼9.2 m. Additionally, the high signal-to-noise ratio (> 50 dB) confirms the stable mode locking.

Further increasing the pump power to 30.8 mW, the breathing SF-BMS can be achieved in the same fiber laser [Figs. 4(g)–4(i)]. An additional set of sub-sidebands between the zero-order and the first-order sidebands appear on the time-averaged spectra. Meanwhile, on the radio frequency spectra of the breathing SF-BMS and its two constituents, apart from the main peak at 22.397 MHz, there are two symmetric frequency sidebands with a separation of ∼2.62 MHz, corresponding to the breathing period of ∼9 RTs.

Considering the limited scanning speed of the optical spectrum analyzer, we utilize the dispersive Fourier transform technique to reveal the real-time spectral dynamics of the breathing SF-BMS[31–36]. For the field autocorrelation evolution shown in Fig. 5(a), the separation between the pulse center and tail evolves periodically, which agrees well with the simulated results in Fig. 2(b). Figures 5(b) and 5(c) display the spectral evolution over 100 and 9 RTs, respectively, where the bicorn structure and sub-sidebands can be clearly observed, indicating that they are not incoherent continuous waves. The peak intensity

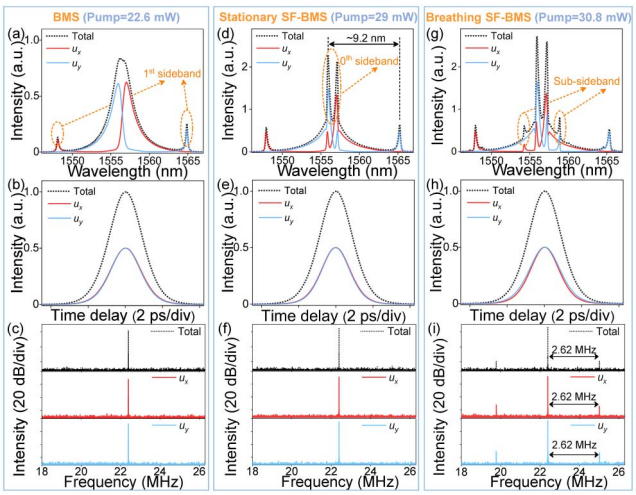

Fig. 4. Laser operation versus the different pump powers. Spectra, autocorrelation traces, and radio frequency spectra for the pump powers of (a)–(c) 22.6 mW, (d)–(f) 29 mW, and (g)–(i) 30.8 mW.

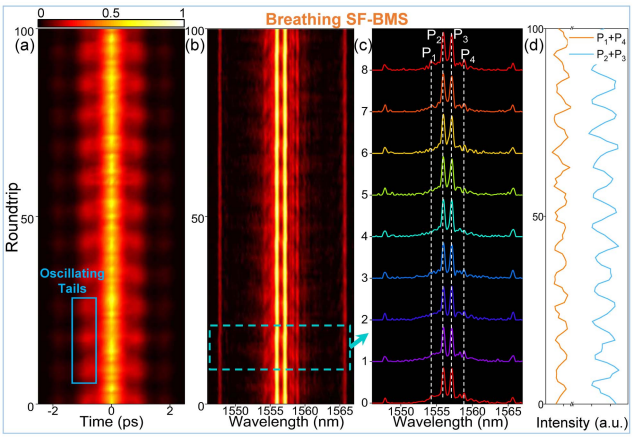

Fig. 5. Experimental results of the breathing SF-BMS. (a) The field autocorrelation and (b) the spectral evolution over 100 RTs. (c) The concrete spectra of the breathing SF-BMS over 9 RTs. (d) The peak intensity evolution for the zero-order sidebands (blue line) and the sub-sidebands (orange line) over 100 RTs.

evolution of the sub-sidebands (peak P_1 and peak P_4) and zero-order sidebands (peak P_2 and peak P_3) is shown in Fig. 5(d), where the peak intensity of the former one increases while that of the latter one decreases, and vice versa. Therefore, the continuous energy exchange between the sub-sidebands and zero-order sidebands is also validated experimentally, which further corroborates the reliability of the above analysis and our simulation model.

6. SF-BMS Achieved in Ytterbium-doped Fiber Laser

Similar SF-BMS can be observed in an all-normal-dispersion birefringence-managed ytterbium-doped fiber (YDF) laser,

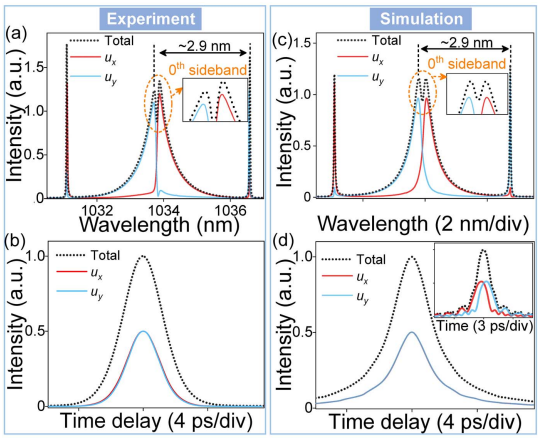

Fig. 6. SF-BMS achieved in all-normal-dispersion YDF lasers. Experimental results: (a) the spectra and (b) the autocorrelation traces for the pump power of 83 mW. Simulation results: (c) the spectra and (d) the autocorrelation traces for the gain saturation energy of 75 pJ. The insets in Figs. 6(a) and 6(c) are close-ups of the bicorn structure. The inset in Fig. 6(d) displays the simulated pulse profiles.

whose cavity length and total dispersion are 8.85 m and 0.217 ps^2, respectively. As illustrated in Figs. 6(a) and 6(b), for the pump power of 83 mW, the SF-BMS displaying a bicorn structure in the spectral center can be obtained. Numerical simulation based on the coupled Ginzburg–Landau equations well reproduces the experimental spectra and autocorrelation traces, as shown in Figs. 6(c) and 6(d). Therefore, the spectral furcation is a ubiquitous phenomenon in birefringence-managed fiber lasers, irrespective of the gain medium and cavity length.

7. Discussion and Conclusion

For the SF-BMS obtained in the normal-dispersion birefringence-managed fiber laser, it goes beyond the traditional consensus that the stationary single-pulse mode-locking state only displays the spectrum possessing one spectral peak without any fine structures, inspiring us to explore solitons with more peculiar spectral structures. Meanwhile, based on the soliton perturbation theory that describes Kelly sidebands in the anomalous-dispersion region[25], when the sideband order is zero, resonant instability inevitably occurs, and the soliton becomes unstable. Therefore, the zero-order sidebands can hardly be observed for the vector soliton in the anomalous-dispersion region, and the stationary spectral furcation is a unique property for the SF-BMS following the birefringence-related phase-matching principle. Moreover, by increasing the pump power, the single-pulse vector solitons in the anomalous-dispersion fiber lasers tend to split into multi-pulses due to the effective gain bandwidth limit[37]. Nonetheless, the bicorn structure of the SF-BMS can be regarded as an energy reservoir, which may provide an effective approach to suppress pulse splitting.

In conclusion, we demonstrate that in normal-dispersion birefringence-managed fiber lasers, two orthogonal-polarized components with sufficiently enhanced zero-order sidebands can trap each other through a reverse frequency shift to form the vector solitons exhibiting bicorn structure in the spectral center. The unequal mode coupling and the birefringence-related phase-matching effect are two critical factors for the generation of the bicorn spectral structure. Such spectral furcation can also be observed in an all-normal-dispersion YDF laser, validating the universality of such spectral furcation in birefringence-managed lasers. Moreover, the formation of the SF-BMS in a normal-dispersion birefringence-managed fiber laser is independent of the total cavity length. Furthermore, the continuous energy exchange between the sub-sidebands and bicorn structure contributes to the breathing dynamics of the SF-BMS, indicating the potential application for optical switch and high bit-rate communications[37]. Our work promotes the understanding of the birefringence-related pulse shaping mechanism, which may spark interest in the exploration of novel vector solitons.

Acknowledgement

This work was supported by the National Natural Science Foundation of China (No. 12274344), the Natural Science Basic Research Program of Shaanxi Province (No. 2021JC-09), and the Fundamental Research Funds for the Central Universities (No. 3102019JC008).

References

1. J. Denschlag, J. E. Simsarian, D. L. Feder, C. W. Clark, L. A. Collins, J. Cubizolles, L. Deng, E. W. Hagley, K. Helmerson, W. P. Reinhardt, S. L. Rolston, B. I. Schneider, and W. D. Phillips, "Generating solitons by phase engineering of a Bose-Einstein condensate," Science **287**, 97 (2000).
2. N. J. Zabusky and M. D. Kruskal, "Interaction of "solitons" in a collisionless plasma and the recurrence of initial states," Phys. Rev. Lett. **15**, 240 (1965).
3. B. Semelin, N. Sánchez, and H. J. de Vega, "Self-gravitating fluid dynamics, instabilities, and solitons," Phys. Rev. D **63**, 084005 (2001).
4. S. Yang, Q.-Y. Zhang, Z.-W. Zhu, Y.-Y. Qi, P. Yin, Y. Q. Ge, L. Li, L. Jin, L. Zhang, and H. Zhang, "Recent advances and challenges on dark solitons in fiber lasers," Opt. Laser Technol. **152**, 108116 (2022).
5. K. Dey and S. Roy, "Analyzing spectral properties and sensing performance of multi-single-multi mode fiber combination," Phys. Scripta **97**, 125507 (2022).
6. F. M. Knox, W. Forysiak, and N. J. Doran, "10-Gbt/s soliton communication systems over standard fiber at 1.55 μm and the use of dispersion compensation," J. Lightwave Technol. **13**, 1955 (1995).
7. P. Grelu and N. Akhmediev, "Dissipative solitons for mode-locked lasers," Nat. Photonics **6**, 84 (2012).
8. M. E. Fermann and I. Hartl, "Ultrafast fibre lasers," Nat. Photonics **7**, 868 (2013).
9. K. Tamura, L. E. Nelson, H. A. Haus, and E. P. Ippen, "Soliton versus nonsoliton operation of fiber ring lasers," Appl. Phys. Lett. **64**, 149 (1994).
10. K. Tamura, E. P. Ippen, and H. A. Haus, "Pulse dynamics in stretched-pulse fiber lasers," Appl. Phys. Lett. **67**, 158 (1995).
11. J. M. Dudley, C. Finot, D. J. Richardson, and G. Millot, "Self-similarity in ultrafast nonlinear optics," Nat. Phys. **3**, 597 (2007).
12. H. Liu, Z. Liu, E. S. Lamb, and F. Wise, "Self-similar erbium-doped fiber laser with large normal dispersion," Opt. Lett. **39**, 1019 (2014).
13. W. H. Renninger, A. Chong, and F. W. Wise, "Dissipative solitons in normal-dispersion fiber lasers," Phys. Rev. A **77**, 023814 (2008).
14. S. T. Cundiff, B. C. Collings, N. N. Akhmediev, J. M. Soto-Crespo, K. Bergman, and W. H. Knox, "Observation of polarization-locked vector solitons in an optical fiber," Phys. Rev. Lett. **82**, 3988 (1999).
15. C. R. Menyuk, "Stability of solitons in birefringent optical fibers. I: equal propagation amplitudes," Opt. Lett. **12**, 614 (1987).
16. M. N. Islam, C. D. Poole, and J. P. Gordon, "Soliton trapping in birefringent optical fibers," Opt. Lett. **14**, 1011 (1989).
17. D. Mao, X. Liu, and H. Lu, "Observation of pulse trapping in a near-zero dispersion regime," Opt. Lett. **37**, 2619 (2012).
18. H. Zhang, D. Y. Tang, L. M. Zhao, and N. Xiang, "Coherent energy exchange between components of a vector soliton in fiber lasers," Opt. Express **16**, 12618 (2008).
19. D. Y. Tang, H. Zhang, L. M. Zhao, and X. Wu, "Observation of high-order polarization-locked vector solitons in a fiber laser," Phys. Rev. Lett. **101**, 153904 (2008).
20. P. Cheng, M. Han, Y. Du, and X. Shu, "Polarization domains and self-mode-locked pulses in an erbium-doped fiber laser," Chin. Opt. Lett. **21**, 031402 (2023).
21. A. E. Akosman, J. Zeng, P. D. Samolis, and M. Y. Sander, "Polarization rotation dynamics in harmonically mode-locked vector soliton fiber lasers," IEEE J. Sel. Top. Quantum Electron. **24**, 110107 (2018).
22. L. M. Zhao, D. Y. Tang, X. Wu, H. Zhang, and H. Y. Tam, "Coexistence of polarization-locked and polarization-rotating vector solitons in a fiber laser with SESAM," Opt. Lett. **34**, 3059 (2009).
23. D. Mao, Z. He, Y. Zhang, Y. Du, C. Zeng, L. Yun, Z. Luo, T. Li, Z. Sun, and J. Zhao, "Phase-matching-induced near-chirp-free solitons in normal-dispersion fiber lasers," Light Sci. Appl. **11**, 25 (2022).
24. D. Mao, Z. He, Q. Gao, C. Zeng, L. Yun, Y. Du, H. Lu, Z. Sun, and J. Zhao, "Birefringence-managed normal-dispersion fiber laser delivering energy-tunable chirp-free solitons," Ultrafast Science **2022**, 9760631 (2022).

25. L. E. Nelson, D. J. Jones, K. Tamura, H. A. Haus, and E. P. Ippen, "Ultrashort-pulse fiber ring lasers," Appl. Phys. B **65**, 277 (1997).
26. G. P. Agrawal, *Nonlinear Fiber Optics* (Academic Press, 2001).
27. W. He, M. Pang, D.-H. Yeh, J. Huang, and P. St.J. Russell, "Synthesis and dissociation of soliton molecules in parallel optical-soliton reactors," Light Sci. Appl. **10**, 120 (2021).
28. K. Tamura, C. R. Doerr, H. A. Haus, and E. P. Ippen, "Soliton fiber ring laser stabilization and tuning with a broad intracavity filter," IEEE Photon. Technol. Lett. **6**, 697 (1994).
29. A. Komarov, F. Amrani, A. Dmitriev, K. Komarov, D. Meshcheriakov, and F. Sanchez, "Dispersive-wave mechanism of interaction between ultrashort pulses in passive mode-locked fiber lasers," Phys. Rev. A **85**, 013802 (2012).
30. Q. Huang, Z. Huang, and C. Mou, "Transient soliton dynamics in a mode-locked fiber laser: from stationary to pulsation," Opt. Lett. **46**, 5683 (2021).
31. K. Goda and B. Jalali, "Dispersive Fourier transformation for fast continuous single-shot measurements," Nat. Photonics **7**, 102 (2013).
32. A. F. J. Runge, N. G. R. Broderick, and M. Erkintalo, "Observation of soliton explosions in a passively mode-locked fiber laser," Optica **2**, 36 (2015).
33. K. Krupa, K. Nithyanandan, U. Andral, P. Tchofo-Dinda, and P. Grelu, "Real-time observation of internal motion within ultrafast dissipative optical soliton molecules," Phys. Rev. Lett. **118**, 243901 (2017).
34. M. Liu, Z.-W. Wei, H. Li, T.-J. Li, A.-P. Luo, W.-C. Xu, and Z.-C. Luo, "Visualizing the "invisible" soliton pulsation in an ultrafast laser," Laser Photonics Rev. **14**, 1900317 (2020).
35. Z. Zhang, J. Tian, Y. Cui, Y. Wu, and Y. Song, "Dynamics of multi-state in a simplified mode-locked Yb-doped fiber laser," Chin. Opt. Lett. **20**, 081402 (2022).
36. D. Y. Tang, L. M. Zhao, B. Zhao, and A. Q. Liu, "Mechanism of multisoliton formation and soliton energy quantization in passively mode-locked fiber lasers," Phys. Rev. A **72**, 043816 (2005).
37. F. Kurtz, C. Ropers, and G. Herink, "Resonant excitation and all-optical switching of femtosecond soliton molecules," Nat. Photonics **14**, 9 (2020).